PNAS

Supporting Information for
The Electrochemistry of Stable Sulfur Isotopes *versus* Lithium

Xue-Ting Li[a,b,1], Yao Zhao[c,1], Yu-Hui Zhu[a,b], Wen-Peng Wang[a], Ying Zhang[a], Fuyi Wang[c], Yu-Guo Guo[a,b], Sen Xin[a,b,*], Chunli Bai[a,b,*]

[a] CAS Key Laboratory of Molecular Nanostructure and Nanotechnology, CAS Research/Education Center for Excellence in Molecular Sciences, Beijing National Laboratory for Molecular Sciences (BNLMS), Institute of Chemistry, Chinese Academy of Sciences (CAS), Beijing 100190, China

[b] University of Chinese Academy of Sciences, Beijing 100049, China

[c] CAS Key Laboratory of Analytical Chemistry for Living Biosystems, CAS Research/Education Center for Excellence in Molecular Sciences, BNLMS, National Centre for Mass Spectrometry in Beijing, Institute of Chemistry, CAS, Beijing, 100190, China

[1] The authors contributed equally to this work.

* Corresponding author. Sen Xin, Chunli Bai
Email: xinsen08@iccas.ac.cn, clbai@cas.cn

This PDF file includes:

Supporting Information Text

Note S1. Description about Morse potential diagram of $^{32}S_2$ and $^{34}S_2$.

Morse potential, $V(r)$ is a descriptor for intramolecular interaction in a diatomic molecule, and is extensively used for vibrational and rotational band analysis (1, 2). The basic form of Morse potential can be expressed as follows,

$$V(r) = D[\left(1 - e^{-a(r-r_0)}\right)^2 - 1] \quad \text{(S1-1)}$$

Where D denotes the well depth, r denotes the internuclear separation (or interatomic distance), r_0 denotes the interatomic distance at the bottom of well, and a is a parameter that controls the width of the potential well (3).

When the interatomic distance reaches the bottom of well ($r = r_0$), $V(r)$ shows the lowest value of $-D$. When the distance approaches to an infinite value ($r \to \infty$), the value of $V(r)$ approaches to zero, which indicates two separate atoms free of any intramolecular interaction (unbound state).

By substituting the Morse potential into the Schrödinger equation, the analytical solutions for vibrational levels of diatomic molecules can be derived and expressed as follows,

$$\left(-\frac{\hbar}{2\mu}\frac{\partial^2}{\partial r^2} + V(r)\right)\psi = E\psi \quad \text{(S1-2)}$$

The eigenvalues (E_n) for vibrational energy levels are given by

$$E_n = \hbar\omega_0\left(v + \frac{1}{2}\right) - \frac{\left[\hbar\omega_0\left(v+\frac{1}{2}\right)\right]^2}{4D} - D \quad \text{(S1-3)}$$

Where v is the vibrational quantum number, $v = 0, 1, 2, \ldots$

$$\omega_0 = a\sqrt{\frac{D}{\mu}} \quad \text{(S1-4)}$$

And μ is the reduced mass of the two nuclei:

$$\mu = \left(\frac{1}{m_1} + \frac{1}{m_2}\right)^{-1} \quad \text{(S1-5)}$$

According to the Eq. (S1-3), the lowest possible energy of the system at the ground vibrational state ($v = 0$) has an increment of $\frac{1}{2}\hbar\omega_0 - \frac{(\hbar\omega_0)^2}{16D}$ relative to $-D$. This energy is commonly referred to as ZPE, which originates from the ceaseless molecular vibrations even at absolute zero (4). E_d of a diatomic molecule corresponds to the energy for activating the molecule from its ground state to an unbound state, which mathematically equals to the absolute value of difference between $E_{r\to\infty}$ and ZPE.

$$E_d = \left|E_{r\to\infty} - E_0\right| = D - (\frac{1}{2}\hbar\omega_0 - \frac{(\hbar\omega_0)^2}{16D}) \quad \text{(S1-6)}$$

Consequently, a lower ZPE indicates a higher E_d and a higher thermodynamic stability of the molecule. In the case of isotopic molecules, they are usually deemed to share the same Morse potential, as $V(r)$ predominantly reflects the electrostatic interactions (5). Based on the Eqs. (S1-3) to (S1-5), the ZPE is inversely proportional to the square root of the reduced mass μ. Therefore, heavier molecules tend to have a lower vibrational frequency and a lower ZPE, and therefore, a higher E_d. For the isotopic S molecules, the heavier $^{34}S_2$ molecule shows a lower ZPE than the $^{32}S_2$ molecule (ZPE($^{32}S_2$): -7.02 eV > ZPE($^{34}S_2$): -7.15 eV), and a higher bond dissociation energy accordingly.

In addition to E_d, ZPE also accounts for the different bond lengths between isotopic molecules. Anharmonic vibrations would cause asymmetric variations of intermolecular distance in response to molecule elongation and contraction (6). Since the Morse potential curve is flatter in the region $r > r_0$ than $r < r_0$, the molecule elongation attributes more to the intramolecular distance than the molecule contraction, which accounts for an increased bond length at a higher vibrational level. As a result, the $^{32}S_2$ molecules with a higher ZPE also show a larger bond length than $^{34}S_2$ (bond length($^{32}S_2$): 1.90 Å > bond length ($^{34}S_2$): 1.89 Å).

Note S2. Calculation of the theoretical Li storage capacity of the ^{32}S/^{34}S cathode.

For a given electrode reaction,

Ox + ve^- → Red (Ox: oxidative species, Red: reductive species),

the theoretical specific capacity of active material on the electrode can be calculated according to the following formula:

$$C = nF/3.6M, \quad \text{(S2-1)}$$

where C is the specific capacity, n is the charge transfer number, F is the Faraday constant (96485 C/mol) and M is the molar mass of the active material.

For the two-electron reduction reaction of S that occurs during discharge of a Li-S cell,

$S + 2e^- \rightarrow S^{2-}$, Eq. (S2-1) can be further simplified as,

$$C_s = 53603/M, \quad \text{(S2-2)}$$

As the molar mass of ^{32}S (^{34}S) is 32 (34) g/mol, the theoretical specific capacity of ^{32}S (^{34}S) is calculated as 1675 (1576) mAh/g.

Note S3. Molar electron transfer number for Li_2S_2/Li_2S precipitation in a Li-S cell.

The amount of electricity that passes through an electrochemical cell is calculated according to the following Eq. (S3-1):

$$Q = \int_{t_1}^{t_2} i\mathrm{d}t, \quad \text{(S3-1)}$$

where Q is the amount of electric charge, i is the current and t is the time.

According to Fig. 2e-f, the t_{os} for Li_2S precipitation refers to the time of current valley at the end of initial current drop, and is applied as t_1 for Eq. (S3-1). The ending time of the experiment (20000 s) is applied as t_2 for Eq. (S3-1). By calculating the integral area between t_1 and t_2 of the *i-t* profile, the amount of transferred charges during Li_2S_2/Li_2S precipitation is 76732 C per mole ^{32}S and 75670 C per mole ^{34}S. The amount of electricity is then divided by the Faraday constant (F = 96485 C/mol, which denotes the amount of electric charges carried by 1 mole electrons), to yield a molar electron transfer number of 0.797 for ^{32}S and 0.785 for ^{34}S.

Note S4. Calculation of separation factor for ^{32}S/^{34}S isotopes.

The separation factor (α) is usually employed for evaluating the efficiency of isotope separation (7), which is defined by the following equation:

$$\alpha = \frac{x_A/y_A}{x_B/y_B} \quad \text{(S4-1)}$$

where x_A and y_A separately denotes the molar fractions of two isotopes in Phase A, and x_B and y_B separately denotes the molar fractions of two isotopes in Phase B. According to Fig. 3b and 3d, the molar ratio of ^{32}S/^{34}S on the uncycled cathode (Phase B) is 1, while the molar ratio of ^{32}S/^{34}S on the cycled Li-metal anode (Phase A) is 1.1-1.2 after 1 (dis)charge cycle and 1.6-2.0 after 10 (dis)charge cycles. In this way, the value of α for ^{32}S/^{34}S isotopes is calculated to be 1.1-1.2 after 1 (dis)charge cycle and 1.6-2.0 after 10 (dis)charge cycles in a Li-S battery.

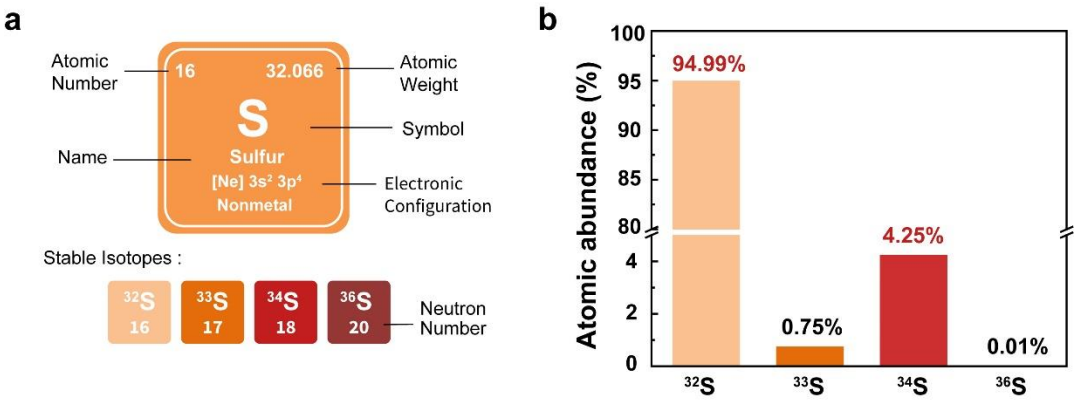

Fig. S1. (a) Basic information of S element from the Periodic Table. (b) Relative atomic abundances of the four stable S isotopes in nature.

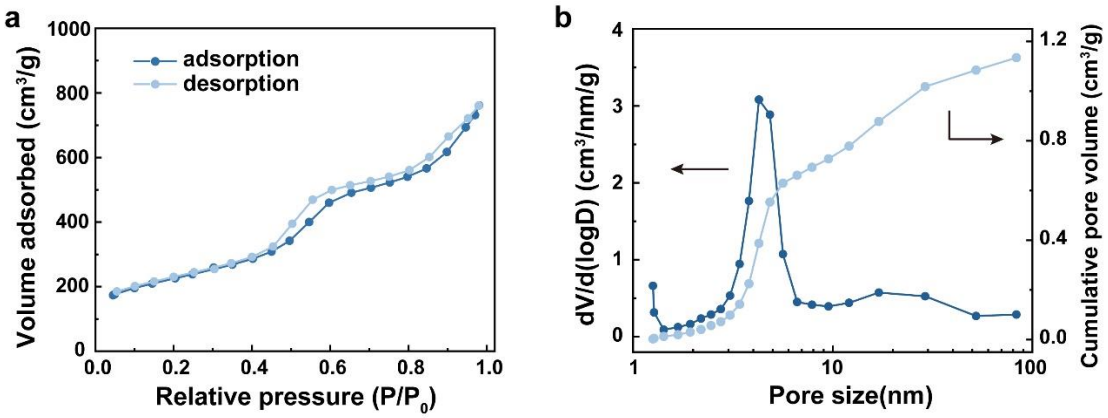

Fig. S2. (a) N_2 adsorption/desorption isotherms of the CMK-3 mesoporous carbon. (b) Pore size distribution and cumulative pore volume calculated by the BJH method of CMK-3.

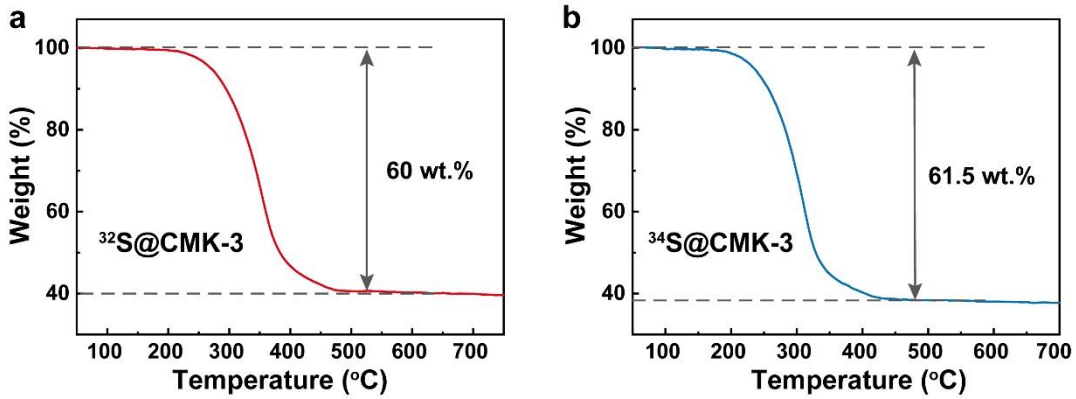

Fig. S3. TG profiles of (a) ^{32}S@CMK-3 and (b) ^{34}S@CMK-3.

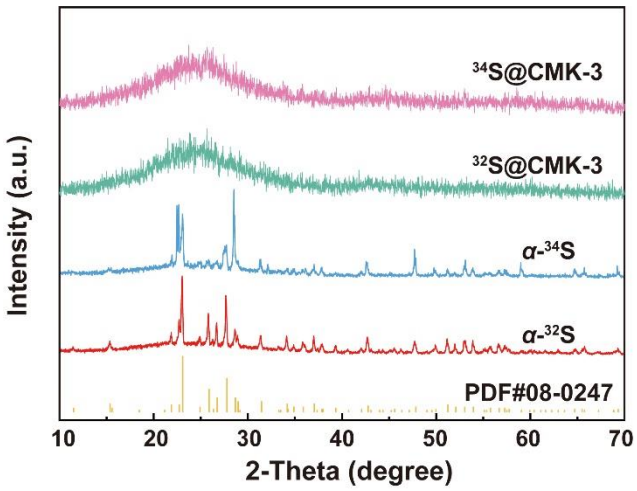

Fig. S4. XRD patterns of ^{34}S@CMK-3, ^{32}S@CMK-3, and rhombic structured *α*-S powder.

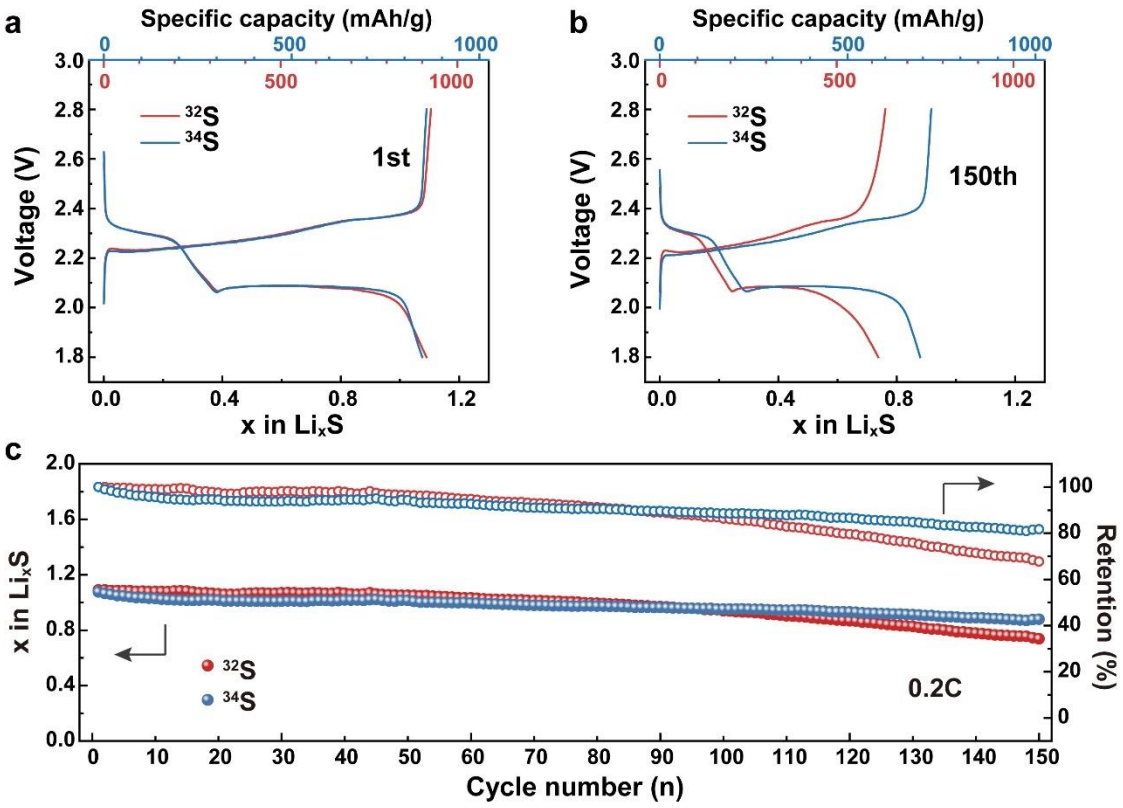

Fig. S5. Electrochemical performance of the Li-^{32}S and Li-^{34}S cells. (a-b) GDC voltage profiles of specific discharge-charge cycles, (c) cycling performance and capacity retention of the cells.

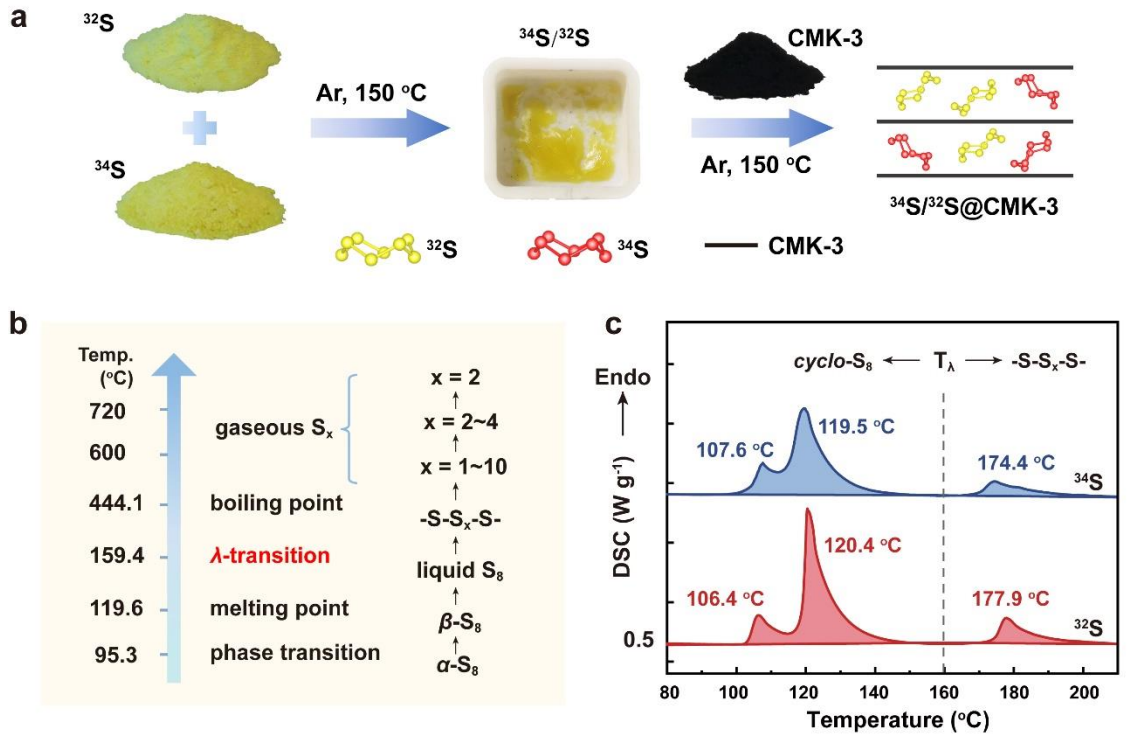

Fig. S6. (a) Preparation of $^{32}S/^{34}S$@CMK-3. (b) Transition of different S forms (in crystals/molecules) by increasing temperature at 1 atm. (c) Thermograms of ^{32}S and ^{34}S powder collected by DSC.

Discussion regarding the various forms of S at 1 atm.

At room temperature, *cyclo*-S_8 molecules exist as a rhombic crystal. A phase transition from *α*-S to monoclinic sulfur (*β*-S) occurs at *ca.* 95.3 °C, and the temperature could vary depending on the heating rate. As the temperature increases to 119.6 °C, *β*-S undergoes a phase transition from a solid state to a liquid state, during which the intermolecular interactions weaken and *cyclo*-S_8 molecules present a disordered arrangement. The ring structure of S_8 molecules persists until 159.4 °C, when the liquid sulfur experiences an abrupt *λ*-transformation that opens the ring structure and turns the *cyclo*-S_8 molecules into chain monomers with one free radical at each end. These monomers then couple together to form a macromolecular sulfur chain (-S-S_x-S-) that consists of, to the maximum content, 200,000 S atoms at *ca.* 180 °C. As a result, the viscosity of liquid sulfur increases instantly by several orders of magnitude. By further increasing the temperature, the polymer S chains gradually depolymerize. When the rate of depolymerization exceeds that of coupled polymerization, a substantial chain-shortening reaction occurs and the liquid S becomes less viscous. At a temperature >444.1 °C, liquid S reaches its boiling point and vaporizes to chain-like S allotropes (S_x, $2 \le x \le 10$). At *ca.* 600 °C, S_8 becomes the major form of allotrope. At 620-720 °C, short-chain-like S allotropes (S_{2-4}) are the major components of vapor. At above 720 °C, S_2 becomes the predominant component (8-12).

Thermoanalysis of ^{34}S and ^{32}S according to SI Appendix, Fig. S6c.

Both sulfur isotopes exhibit similar thermal behavior, with three endothermic peaks observed before 200 °C. The first peak is assigned to the solid-solid transition from *α*-S to *β*-S, and its temperature depends largely on the heating rate: 100 °C at 4 °C/min, 107 °C at 5 °C/min, 111 °C at 10 °C/min, and 113 °C at 20 °C/min (13). The intense peak at ~120 °C is assigned to the melting of *β*-S (into liquid S). Finally, a small endothermic peak at around 175 °C corresponds to the formation of polymer S.

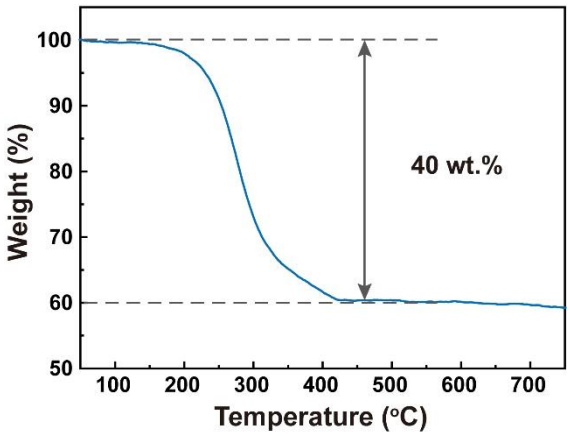

Fig. S7. TG profile of $^{32}S/^{34}S$@CMK-3.

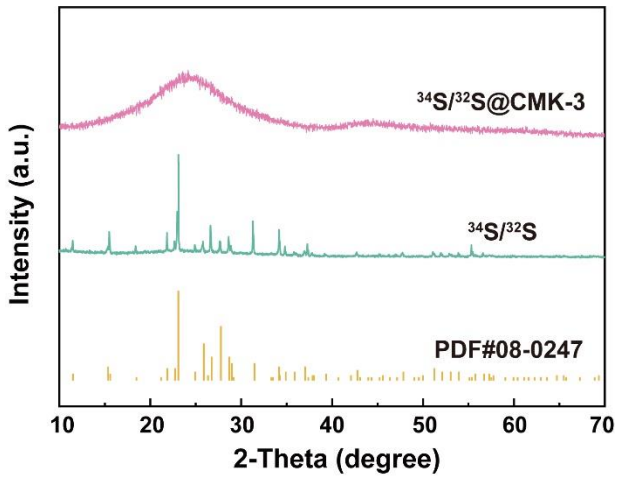

Fig. S8. XRD patterns of $^{34}S/^{32}S$ mixture and $^{32}S/^{34}S$@CMK-3.

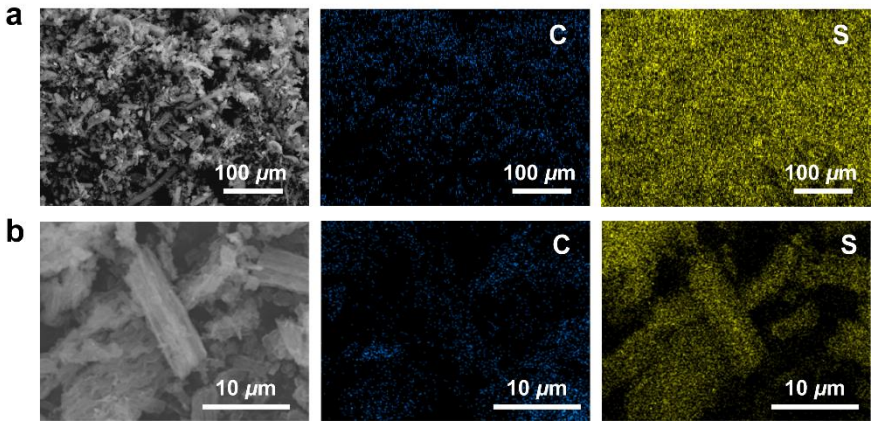

Fig. S9. SEM images and EDS elemental mappings (a) at a low resolution and (b) at a high resolution of $^{32}S/^{34}S$@CMK-3.

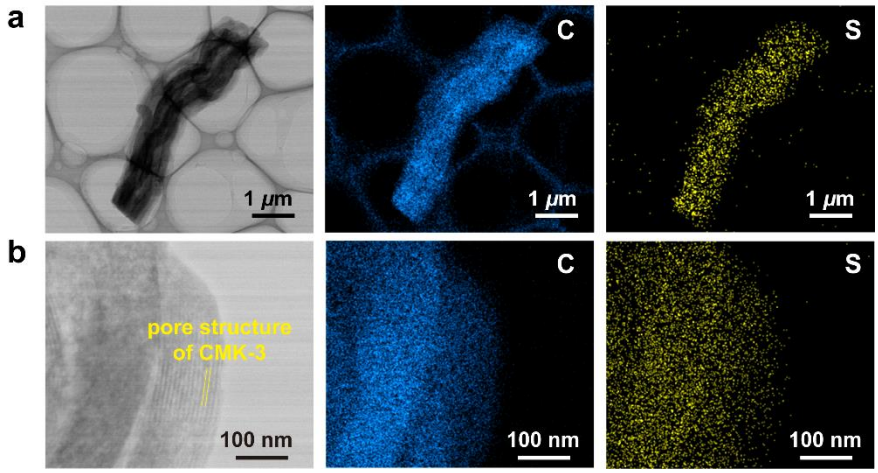

Fig. S10. TEM images and EDS elemental mappings of $^{32}S/^{34}S$@CMK-3.

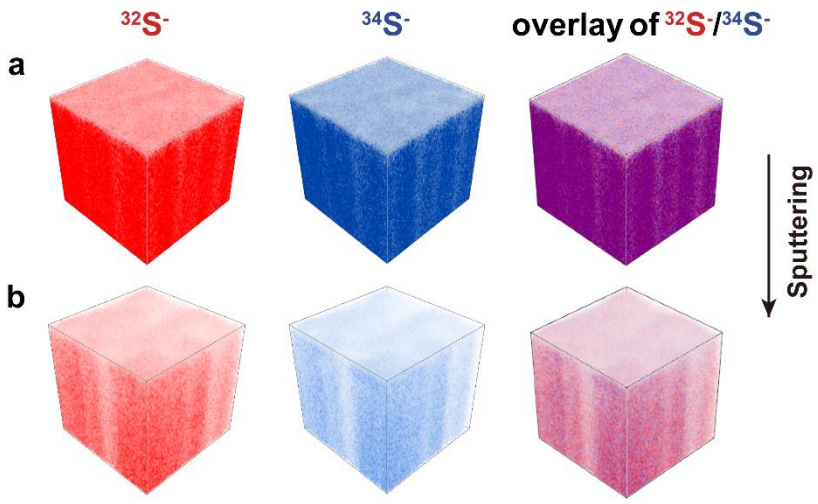

Fig. S11. 3D spatial distribution of isotopic S fragments in (a) the uncycled $^{34}S/^{32}S$@CMK-3 cathode and (b) the cycled Li-metal anode.

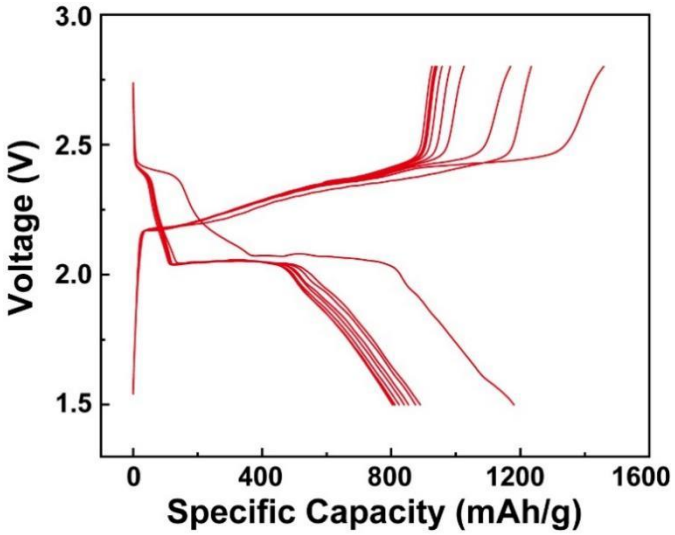

Fig. S12. Typical discharge-charge profiles at 0.1C of the Li-^{34}S/^{32}S@CMK-3 cell.

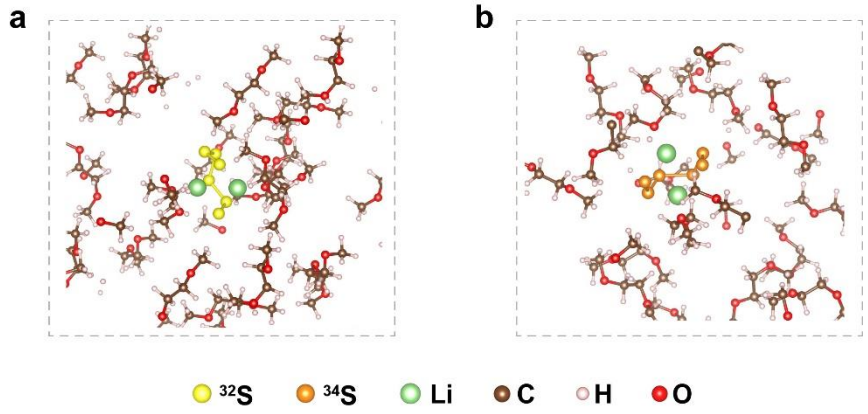

Fig. S13. AIMD snapshots taken from DME-solvated structures of (a) $Li_2{}^{32}S_6$ and (b) $Li_2{}^{34}S_6$.

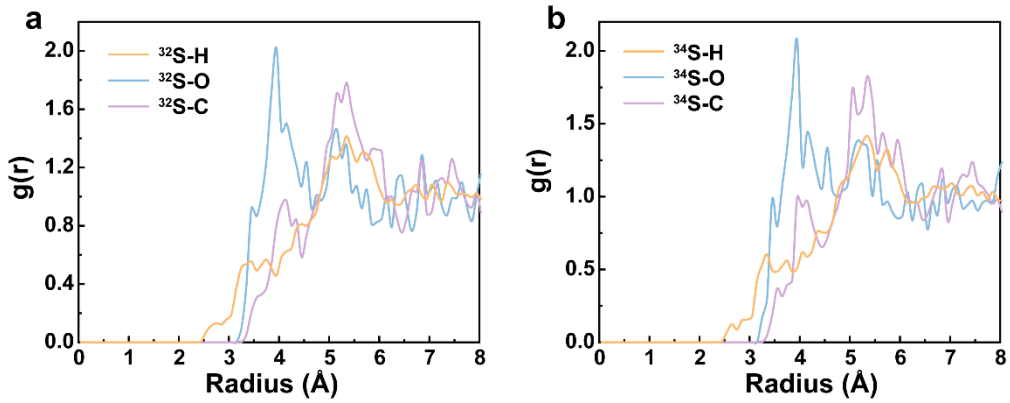

Fig. S14. RDF profiles that describe the anion-solvent interactions via S-X of (a) $Li_2{}^{32}S_6$ and (b) $Li_2{}^{34}S_6$.

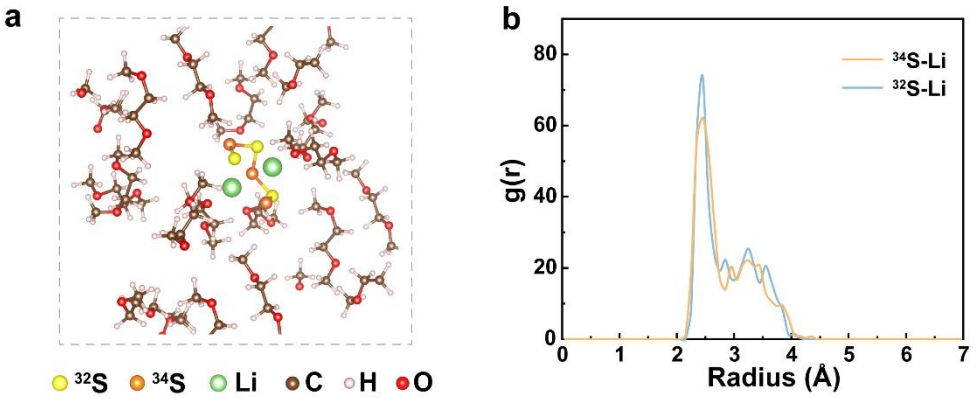

Fig. S15. (a) AIMD snapshot taken from a DME-solvated $Li_2{}^{32}S_3{}^{34}S_3$. (b) RDF profiles that describe the interactions with DME via ^{34}S-Li and ^{32}S-Li.

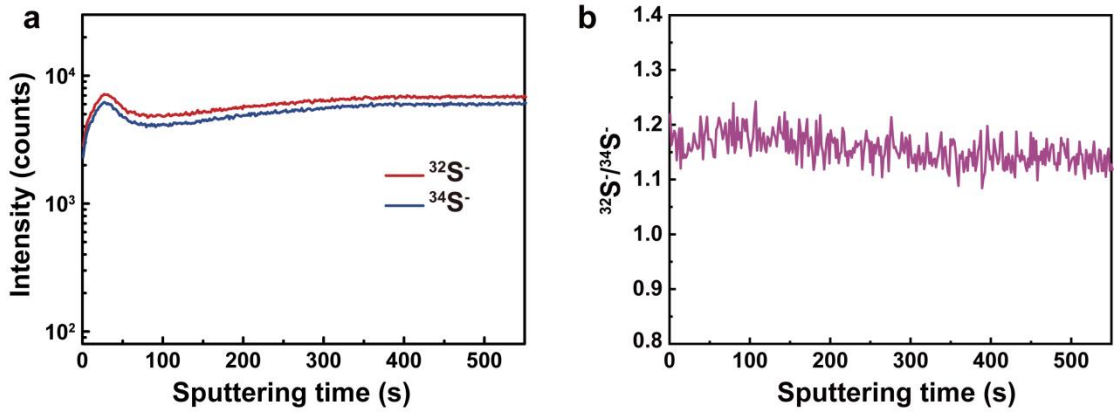

Fig. S16. (a) ToF-SIMS depth profiles of $^{32}S^-$ and $^{34}S^-$ collected from the Li-metal anode of Li-^{34}S/^{32}S@CMK-3 cell after 1 (dis)charge cycle, and (b) variation of $^{32}S^-/^{34}S^-$ intensity ratio with sputtering time.

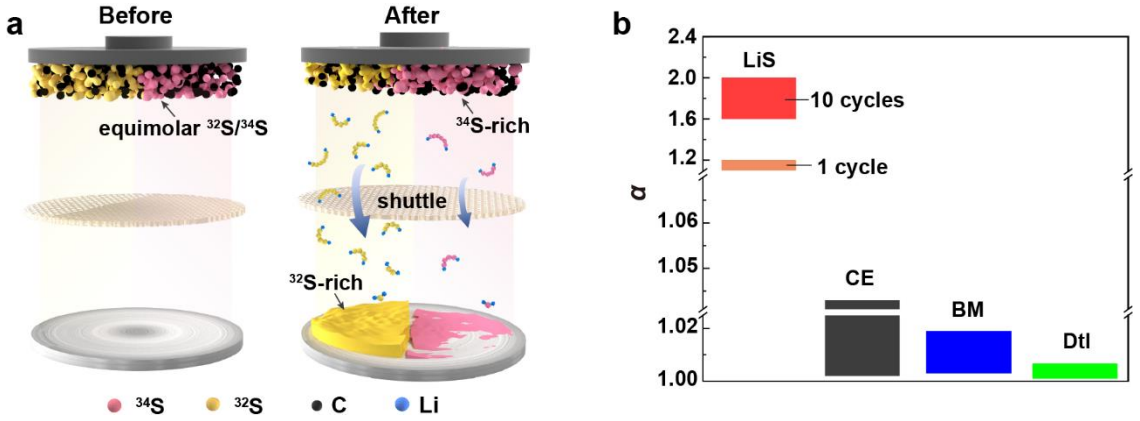

Fig. S17. Electrochemical separation of $^{32}S/^{34}S$ isotopes taking the advantage of LiPS shuttle in a Li-S battery. (a) A schematic showing the principle of isotope separation, where the heavier ^{34}S tends to remain on the cathode, while the lighter ^{32}S tends to migrate to the Li-metal anode after the battery undergoes several discharge-charge cycles. (b) Separation factors for $^{32}S/^{34}S$ isotopes by different methods, including Li-S battery (LiS), chemical exchange (CE), bacterial metabolism (BM) and distillation (Dtl). The calculation of α via Li-S battery is stated in Note S4, and the values via other methods are concluded from references (14-18).

Table S1. Physical properties at a macroscopic level of ^{32}S and ^{34}S.

Property	**^{32}S**	**^{34}S***
Density at 25°C (g cm^{-3})	2.07	2.05
Vapor pressure at 246°C (hPa)	10	10
Melting point (°C)	120.4	119.5
Boiling point (°C)	444.6	444.7
Flashing point (°C)	168	168

*The physical properties of ^{34}S were obtained from the Cambridge Isotope Laboratories, Inc.

Table S2. Key parameters of *cyclo*-$^{32}S_8$ and *cyclo*-$^{34}S_8$ molecules.

Parameter	***cyclo*-$^{32}S_8$**	***cyclo*-$^{34}S_8$**
Bond angle (°)	109.35	109.35
Bond length (Å)	2.06	2.04
ZPE (eV)	-30.17	-32.93

Table S3. Vibrational information of isotopic *cyclo*-S_8 molecules by DFT calculation.

Vibration mode	Vibrational frequency of *cyclo*-$^{32}S_8$ (cm^{-1})	Vibrational frequency of *cyclo*-$^{34}S_8$ (cm^{-1})
1 f	469.99	455.99
2 f	460.50	446.77
3 f	460.36	446.64
4 f	450.48	437.06
5 f	450.46	437.03
6 f	386.36	374.84
7 f	386.34	374.82
8 f	351.25	340.78
9 f	247.80	240.41
10 f	247.72	240.34
11 f	231.53	224.64
12 f	213.70	207.33
13 f	187.54	181.95
14 f	187.36	181.77
15 f	138.29	134.17
16 f	138.09	133.98
17 f	75.58	73.33
18 f	74.71	72.48
19 f	11.31	10.97
20 f	1.01	0.98

Table S4. Maximum mass loading* of S isotopes in the CMK-3 carbon.

Property	**^{32}S**	**^{34}S**
Density at 25°C (g/cm^3)	2.07	2.05
Maximum S mass loading per gram CMK-3 (g)	2.35	2.33
Maximum mass percentage of S in S@CMK-3 (wt.%)	70.1	69.9

*The CMK-3 carbon shows a cumulative pore volume of **1.135 cm^3/g** based on the BJH method (SI Appendix, Fig. S2). The maximum S mass loading per gram CMK-3 was calculated by multiplying the pore volume of CMK-3 and the density of sulfur isotope.

Table S5. Polarization voltages* collected during the GITT test of Li-^{32}S and Li-^{32}S cells.

x in Li_xS	Li-^{32}S	Li-^{34}S
0.1	0.0505	0.0481
0.2	0.1727	0.1699
0.3	0.0983	0.0862
0.4	0.0753	0.0704
0.5	0.0756	0.0722
0.6	0.0778	0.0726
0.7	0.0747	0.0713
0.8	0.0766	0.0735
0.9	0.0800	0.0779
1	0.0849	0.0828
1.1	0.0927	0.0973
1.2	0.1137	0.1873
1.3	0.2824	0.3268
1.4	0.3547	0.3624

*The voltage values were obtained by subtracting the discharge voltage from the equilibrium voltage at the SOC.

Table S6. Molar ratio of ^{32}S to ^{34}S in cycled electrolyte measured by ICP-MS.

Sample name	**^{32}S (CPS*)**	**^{34}S (CPS)**	**$^{32}S/^{34}S$**
Background	2.764×10^{6}	1.215×10^{5}	——
Standard liquid	6.958×10^{6}	3.257×10^{5}	20.54
Correction factor		**1.128****	
Blank sample	1.150×10^{7}	5.404×10^{5}	——
Sample 1	2.780×10^{7}	1.045×10^{7}	**1.86****
Sample 2	2.526×10^{7}	1.079×10^{7}	**1.52****
Sample 3	3.166×10^{7}	1.171×10^{7}	**2.04****

*CPS is short for counts per second.

**The bolded numbers are calculated from the original data.
I. The $^{32}S/^{34}S$ ratio of standard liquid (20.54) is obtained after subtracting the background signal.
II. The correction factor is the ratio of thestandard $^{32}S/^{34}S$ value (23.17) to the tested value (20.54).
III. The $^{32}S/^{34}S$ ratio of the tested sample is obtained after deducting the signal of the blank sample and multiplying it by the correction factor.

Table S7. Solvation energy (eV) for different LiPS species in DME.

	Li_2S_8	Li_2S_6	Li_2S_4
^{32}S	-0.158	- 0.144	- 0.126
^{34}S	- 0.180	- 0.166	- 0.145

Table S8. Parameters of 10-Ah Li-S pouch cells. A negative to positive (N/P) ratio of 1.5, an electrolyte to S (E/S) ratio of 2 μL/mg, an average voltage of 2.1 V, and theoretical specific capacities of ^{34}S (1576 mAh/g), ^{32}S (1675 mAh/g) and Li (3860 mAh/g) were employed for calculating the battery energy. The Li-^{34}S pouch cell shows a specific energy of 452 Wh/kg, which is ~2.6% lower than that of the Li-^{32}S cell (464 Wh/kg).

	Parameter	Li-^{32}S	Li-^{34}S
Cathode	Specific Capacity of S (mAh/g)	1675	1576
	Mass Ratio of Active S (wt.%)	80	80
	Areal Capacity (mAh/cm^2)	6	6
	Areal S Weight (mg/cm^2)	3.58	3.81
	Number of Cathode Pieces	12	12
Anode	Specific Capacity of Li (mAh/g)	3860	3860
	Areal Capacity (mAh/cm^2)	9	9
	Areal Li Weight (mg/cm^2)	2.33	2.33
	Number of Anode Pieces	13	13
Anode Collector	Cu Foil Thickness (μm)	5	5
Cathode Collector	Al Foil Thickness (μm)	13	13
Electrolyte	Injection Mass (g)	12.7	13.6
	E/S Ratio (μL/mg)	2	2
Other Components	Mass (g)	9.1	9.1
Cell	Average Voltage (V)	2.1	2.1
	Designed Capacity (Ah)	10.3	10.3
	Total Mass (g)	46.61	47.88
	Gravimetric Energy Density (Wh/kg)	464	452

SI References

1. J. R. Walton, L. A. Rivera-Rivera, R. R. Lucchese, J. W. Bevan, Morse, Lennard-Jones, and Kratzer Potentials: A canonical perspective with applications*, J. Phys. Chem. A* **120,** 8347-8359 (2016).
2. E. D. German, A. M. Kuznetsov, Theory of the kinetic isotope effect. Use of the Morse potential*, Journal of the Chemical Society, Faraday Transactions 2: Molecular and Chemical Physics* **77,** 2203-2212 (1981).
3. P. M. Morse, Diatomic molecules according to the wave mechanics. II. Vibrational levels*, Phys. Rev.* **34,** 57-64 (1929).
4. T. H. Boyer, Quantum zero-point energy and long-range forces*, Annals of Physics* **56,** 474-503 (1970).
5. J. L. Dunham, The energy levels of a rotating vibrator*, Phys. Rev.* **41,** 721-731 (1932).
6. E. Roduner, "Muonium—An ultra-light isotope of hydrogen" in Isotope Effects In Chemistry and Biology, A. Kohen, H.-H. Limbach, Eds. (CRC Press, 2005), pp. 433-448.
7. E. D. North, R. R. White, Separation of the stable isotope of sulfur 34*, Ind. Eng. Chem.* **43,** 2390-2397 (1951).
8. J. Ruiz-Garcia, E. M. Anderson, S. C. Greer, Shear viscosity of liquid sulfur near the polymerization temperature*, J. Phys. Chem.* **93,** 6980-6983 (2002).
9. B. Yuan, B. Aitken, S. Sen, Is the lambda-transition in liquid sulfur a fragile-to-strong transition?*, J. Chem. Phys.* **151,** 041105 (2019).
10. G. O. Sofekun, E. Evoy, K. L. Lesage, N. Chou, R. A. Marriott, The rheology of liquid elemental sulfur across the *λ*-transition*, J. Rheol.* **62,** 469-476 (2018).
11. M. J. Stashick, R. A. Marriott, Viscoelastic behavior corresponding to reptative relaxation times across the lambda-transition for liquid elemental sulfur*, J. Chem. Phys.* **152,** 044503 (2020).
12. N. N. Greenwood, A. Earnshaw, "Sulfur" in Chemistry of the Elements, (Butterworth-Heinemann, 1997), pp. 645-665.
13. F. W. H. Kruger, W. J. McGill, A DSC study of curative interactions. I. The interaction of ZnO, sulfur, and stearic acid*, J. Appl. Polym. Sci.* **42,** 2661-2667 (1991).
14. T. E. Eriksen, Sulfur isotope effects*, Acta Chem. Scand* **26,** 11 (1972).
15. M. A. Boris, A. S. Polevoi, Separation of sulphur isotopes by physicochemical methods*, Russ. Chem. Rev.* **52,** 213 (1983).
16. T. R. Mills, Practical sulfur isotope separation by distillation*, Sep. Sci. Technol.* **25,** 1919-1930 (1990).
17. L. A. Chambers, P. A. Trudinger, Microbiological fractionation of stable sulfur isotopes: A review and critique*, Geomicrobiol. J.* **1,** 249-293 (1979).
18. D. E. Canfield, B. Thamdrup, The production of ^{34}S-depleted sulfide during bacterial disproportionation of elemental sulfur*, Science* **266,** 1973-1975 (1994).